Composite Structures 306 (2023) 116582

Contents lists available at ScienceDirect

Composite Structures

journal homepage: www.elsevier.com/locate/compstruct

Quasi-static compressive behavior and energy absorption of novel cellular structures with varying cross-section dimension

Ting Li [a], Jian Sun [b], Jinsong Leng [b], Yanju Liu [a,*]

[a] Department of Astronautical Science and Mechanics, Harbin Institute of Technology (HIT), P.O. Box 301, No. 92 West Dazhi Street, Harbin 150001, PR China
[b] Center for Composite Materials and Structures, Science Park of Harbin Institute of Technology (HIT), P.O. Box 3011, No. 2 YiKuang Street, Harbin 150080, PR China

ARTICLE INFO

Keywords:
In-plane compression
Energy absorption
Cellular structure
Mechanical behavior
Variable stiffness

ABSTRACT

Cellular structures exhibit attractive mechanical properties like lightweight, high specific stiffness, and excellent energy absorption. Materials and structures design offers valuable enhancement of nature honeycombs. This work proposed a variable cross-section unit cell to improve compressive and energy absorption properties of the cellular structure constituting these unit cells. In the developed variable cross-section unit cell, the inclined cell walls of the traditional accordion honeycomb were flipped at an angle in the out-of-plane direction or swept along a cousin wave path. The Fused Deposition Modeling (FDM) technique was employed to prepare honeycomb specimens from polylactic acid (PLA). In-plane quasi-static compressive tests were carried out to investigate mechanical behavior and energy absorption of the designed honeycomb structures. The results indicate that the design of the variable cross-section in the width direction enhanced compressive strength and improved energy absorption capability. Based on the variable stiffness characteristic of PLA, isothermal compression experiments were conducted to investigate the temperature dependence of the compressive behavior. This work provides a demonstration for improving the mechanical performance and energy absorption of lightweight cellular structures.

1. Introduction

Honeycomb structures have proven lightweight, high specific stiffness, and extraordinary energy dissipation capabilities [1,2], used as protective structures to resist impact and absorb energy in engineering fields such as aerospace [3], automotive [4–6], and marine applications [7]. Honeycombs are often applied to the core structure of cushioning devices for protection. The densification strain and plateau stress are essential parameters that influence the energy absorption of the honeycomb structures. A typical energy absorbing cellular structure experiences the elastic stage, plateau stress region, and densification stage under compressive loading [8]. The cell walls bend during the initial compression generating a linear elastic deformation. When the stress reaches a certain level, called the plateau stress, the cell wall begins to collapse under plastic yielding or brittle fracture, determined by the material properties. Honeycomb structures absorb most of the energy at the plateau stress region. All cell walls crushing and contacting then enter the densification stage, where the compressive stress raises rapidly [9].

Due to honeycomb structures presenting excellent mechanical properties and energy absorption capability, extensive research has been carried out on structural design and property investigation in recent years. A significant part of the excellent work focuses on the in-plane topology design of cellular structures, such as re-entrant auxetic honeycombs [10–12], double-arrowhead [13,14], star shape[15,16], curved cell walls[17], chiral and anti-chiral honeycombs[18–20]. These honeycomb structures also feature negative Poisson's ratios by experiencing lateral contraction when compressed longitudinally. The other is to complicate the honeycomb configuration for reinforcing the compression performance, such as hybrid honeycomb[16,21–26], foam-filled honeycombs[27,28], self-similar honeycombs[29–31], bamboo biomorphic structure[32]. The gradient honeycomb structures were designed to regulate the compression sequence[33–35]. The above studies share a common feature that the out-of-plane direction is consistent. In addition, several works concentrating on out-of-plane variations of honeycomb structures have appeared recently. For example, the combination re-entrant honeycomb and origami to obtain a three-dimensional negative Poisson's ratio effect[36]. Honeycombs twisted along the axial direction[37], honeycomb structures designed by biomimetic structures[38] were reported. The out-of-plane properties of

* Corresponding author.
E-mail address: yj_liu@hit.edu.cn (Y. Liu).

https://doi.org/10.1016/j.compstruct.2022.116582
Received 13 April 2022; Received in revised form 15 November 2022; Accepted 6 December 2022
Available online 11 December 2022

these honeycomb structures are transformed. The literature review reveals that few studies have investigated mechanical properties and energy absorption performance of honeycomb structures varying along out-of-plane orientations.

Conventional techniques to manufacture honeycombs have several limitations. Honeycomb structures fabricated by conventional techniques have relatively simple topologies generally. Each unit cell type requires a different fabrication process. The size and precision of the honeycombs are not always precisely controlled. The emergence and development of additive manufacturing, or 3D printing technology, have promoted the realization of diversified designs of honeycomb structures. 3D printing technology can freely design geometric shapes and precisely control the printing size. Complex geometrical shapes could be fabricated quickly and adjust geometrical dimensions[39–43]. In addition, 3D printing technology has broken through the design diversity of honeycomb materials, such as alloys[10,29], stainless steel [37], polymer materials[38,44], short carbon fiber reinforced composites[45,46], continuous carbon fiber enhanced composites[47–49]. Fused deposition modeling (FDM) is a popular and effective printing method among additive manufacturing techniques. Thermoplastic shape memory polylactic acid (PLA) possesses high strength and suits for FDM printing. Thermal-responsive PLA material could vary stiffness stimulated by temperature, so its mechanical properties are tunable by temperature[50].

In the present work, we aim to improve the load-bearing and energy absorption performance and develop a novel design of cellular structures that combines additive manufacturing technology. Honeycomb structures with varying cross-section dimensions in the out-of-plane direction were proposed. The in-plane compression behavior and energy absorption performance of designed honeycombs were investigated. Based on the conventional accordion honeycomb, the inclined cell walls were flipped out-of-plane by an angle or swept along with a cousin wave path. The compression specimens were prepared by FDM printing and subjected to quasi-static compression tests. The compression process at room temperature was simulated by finite element simulation. The effects of unit cell configuration, flip angle, and symmetry mode on compressive behavior and energy absorption performance were analyzed. Besides, the novel honeycombs' temperature-dependent mechanical behavior and energy absorbing characteristics were captured by comparing the isothermal compression experiments at several temperatures.

2. Design and experiments

2.1. Honeycomb design

The honeycomb design is based on a hexagonal accordion honeycomb geometric topology. Fig. 1 shows the five representative cells of the novel honeycomb structures with varying cross-sectional dimensions along the out-of-plane direction. The first representative cell is obtained by flipping the inclined cell walls above and below the horizontal wall by the angle θ toward the same out-of-plane direction. This case is recorded as a completely flipped (CF) cell. The reversed flipped (RF) cell is created by flipping the upper and lower walls in the opposite direction. The third type is to flip the inclined cell wall above the horizontal wall, called the partially flipped (PF) cell. In addition, the completely wave cell (CW) and the reversed wave cell (RW) are achieved by sweeping the out-of-plane path of both upper and lower inclined walls like a cosine wave. Compared with the traditional accordion honeycomb, the in-plane topologies of the designed variable-section honeycomb remain unchanged. However, a newly introduced cross-section parameter (out-of-plane flip angle or cosine wave amplitude) breaks the uniformity of the out-of-plane direction. The geometric parameters of the accordion honeycomb cells are denoted by the following symbols: l and t are the length and thickness of the inclined cell walls, respectively. φ represents the inclination angle between the horizontal wall and the inclined wall, and the intercept of the inclined cell wall and the horizontal cell wall is l_1. The total cell length and width are marked as λl and b, respectively. The cell height is $4l\cos\varphi + 2t$. Except for the same geometric parameters described above, additional parameters of five derived cellular structures are the flip angle θ and the cosine wave amplitude a.

The relative density is an essential indicator for evaluating the honeycomb properties, defined as the ratio of the honeycomb density to the parent material density. The slight difference between unit cells shown in Fig. 1 alters the relative density. Here, the relative density $\bar{\rho}$ is

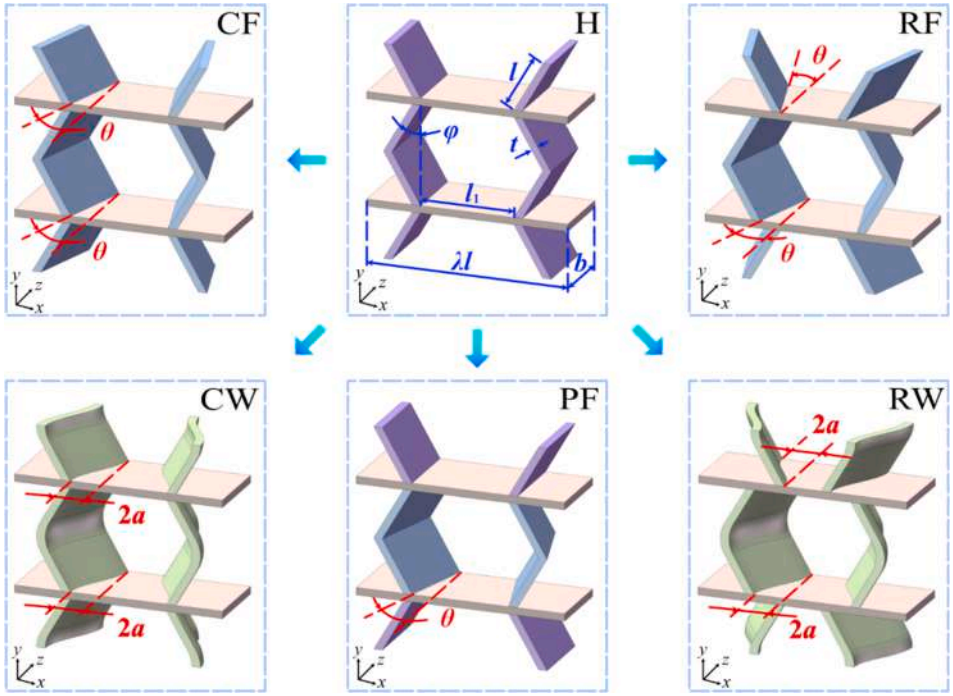

Fig. 1. Representative cell design of novel variable cross-section honeycomb structures.

calculated by dividing the volume of cell walls by the volume of honeycomb, as follows:

$$\begin{cases} \overline{\rho}_H = \dfrac{\lambda+4}{\lambda(1+2l\cos\varphi/t)} \\ \overline{\rho}_{PF} = \dfrac{\lambda+2+2/\cos\theta}{\lambda(1+2l\cos\varphi/t)} \\ \overline{\rho}_{CF}(\overline{\rho}_{RF}) = \dfrac{\lambda+4/\cos\theta}{\lambda(1+2l\cos\varphi/t)} \\ \overline{\rho}_{CW}(\overline{\rho}_{RW}) = \dfrac{\lambda+\dfrac{4}{b}\displaystyle\int_0^b \sqrt{1+\frac{a^2\pi^2}{b^2}\sin^2\left(\frac{\pi}{b}x\right)}\,dx}{\lambda(1+2l\cos\varphi/t)} \end{cases} \tag{1}$$

The designed unit cells' periodic arrangement and symmetrical operation form a honeycomb structure with variable cross-section along the width direction, as shown in Fig. 2. Considering that the variation along the width direction leads to different cellular structures constructed by forwarding and backward symmetry, the effects of symmetry modes on honeycomb structure's compression behavior and energy absorption are investigated. The designed symmetry modes are: 1) Forward and backward symmetry modes, respectively, resulting in a honeycomb with twice the unit cell width (CF-2–1 and CF-2–2 in Fig. 2); 2) Simultaneously forward and backward symmetric modes, obtaining a honeycomb with three times the unit cell width (CF-3 in Fig. 2); 3) Double the honeycombs in 1) to get honeycombs with four times the unit cell width, respectively (CF-4–1 and CF-4–2 in Fig. 2).

Abbreviations rules are arranged by unit cell topology-flip angle-how times of cell width-symmetry mode. For example, CF15-2–2 represents a completely flipped honeycomb with a flip angle of 15°, two times of cell width, and backward symmetry mode. Table 1 lists the unit cell s geometry parameters and specimens overall dimensions (length, width, height). The designed variable-section honeycomb specimens were fabricated by FDM printing technology and printed layer by layer along the width direction. Honeycombs with different flip angles were prepared for the compression tests.

2.2. Parent material properties

Uniaxial tensile experiments were conducted to investigate the mechanical properties of the parent material. Dumbbell-shaped tensile specimens (type Ⅳ) were printed and tested according to ASTM standard D638. The printing direction of the tensile specimens was set to ± 45° filling pattern as PLA specimens exhibited the maximum deformation elongation under tensile loads at this setup[51]. The previous study has characterized the glass transition temperature of the matrix material [52]. Since the load-bearing capability of the parent material exhibited temperature dependence, the tensile experiments were carried out at room temperature and ranged temperature from 35 °C to 60 °C with 5 °C each interval. The Zwick/Rolle universal testing machine with a temperature chamber was used for quasi-static tensile tests. The specimen should be held in the temperature chamber for 20 min to ensure uniform heating before uniaxial stretching. Then the test was carried out at a load rate of 2 mm/min. Three specimens were tested under each temperature condition. The nominal stress is the ratio of the real-time tensile load to the initial cross-section of the tensile specimen, and the nominal strain is the ratio of the displacement to the initial distance between clamps. Engineering stress and engineering strain are calculated by the formulas:

$$\begin{cases} \sigma_{engineering} = \sigma_{nominal}(1+\varepsilon_{nominal}) \\ \varepsilon_{engineering} = \ln(1+\varepsilon_{nominal}) \end{cases} \tag{2}$$

Fig. 3(a) plots the engineering stress–strain curves at different temperatures. The relationship between elastic modulus and temperature is obtained by linear fitting of the curves, as shown in Fig. 3(b). It can be observed that the parent material exhibits variable stiffness properties, the elastic modulus decreasing by three orders of magnitude with the temperature increasing from room temperature to around the glass transition temperature. The modulus dropped drastically between 45 and 55 °C. The parent material exhibits brittle fracture at room temperature, and the elongation at break increases gradually with increasing temperature.

2.3. Quasi-static compression tests

Quasi-static compression tests at room temperature were performed

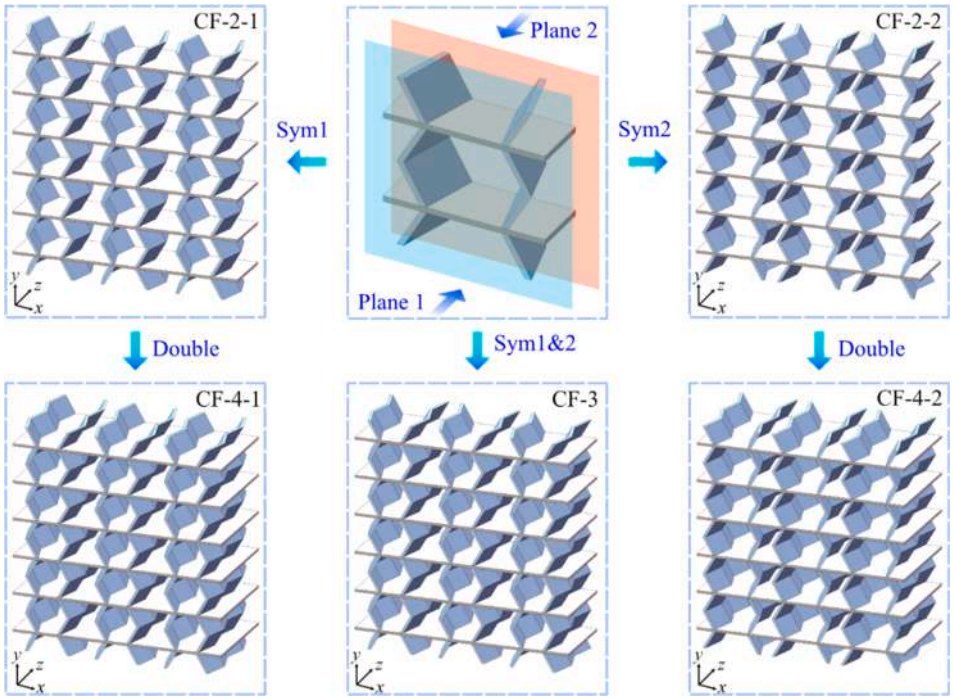

Fig. 2. Demonstration of symmetry mode design.

Table 1
Dimensions of unit cells and honeycombs.

Cell type	Unit cell geometries						Characteristic dimensions		Relative density	Global dimensions		
	l (mm)	t (mm)	φ (°)	l_1 (mm)	λ	b (mm)	θ (°)	a (mm)	$\bar{\rho}$	L (mm)	D (mm)	H (mm)
H							0	–	0.157			
CF/RF	8	1	30	13	2.8	10	15	–	0.160		20	
							30		0.171	84	30	90
PF							30	–	0.164		40	
CW/RW							–	2	0.165			

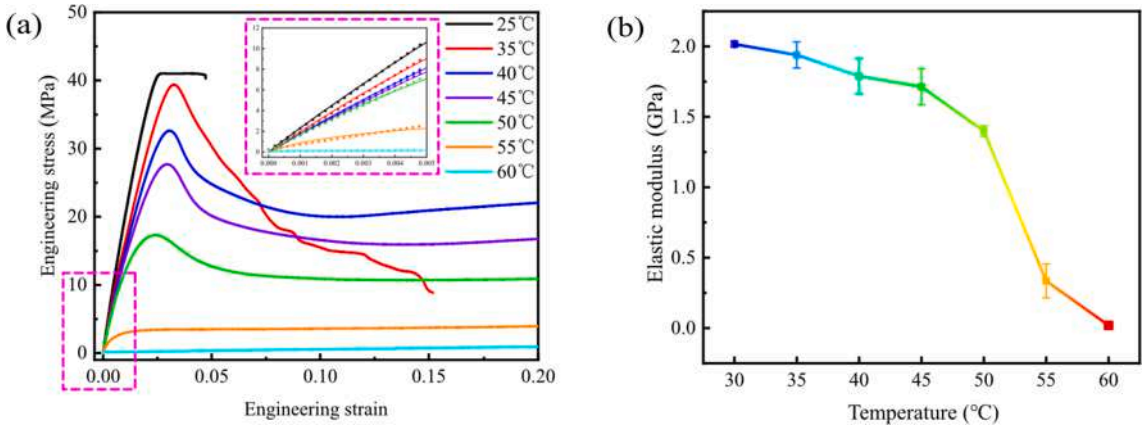

Fig. 3. Tensile properties of parent materials at different temperatures: (a) Engineering stress–strain curves and (b) elastic modulus versus temperatures.

using a Zwick/Rolle universal testing machine. Three repeated uniaxial quasi-static compressive tests of each honeycomb structure were conducted. The honeycomb samples were placed on the fixed platform at the bottom of the testing machine. The movable platen traveled downward at 4 mm/min following ASTM standard D1621 to apply displacement loading. The termination of the compression process was controlled by displacement. Tests ended when each specimen was compressed to 75 % of the honeycomb's height (67.5 mm). A camera was placed in front of the test machine to record the compression process. The primary compression test procedures were the same under different temperatures, except samples had to be heated in the temperature chamber for 20 mins before the compression program started.

2.4. Finite element simulation

The Explicit package of commercial software ABAQUS 2016 was employed to simulate the deformation behavior of the variable cross-section honeycomb structures under quasi-static compression at room temperature. Three representative honeycomb types were selected to perform Finite element (FE) simulations for compressive failure mode analysis and comparison with the experimental results. The FE model consisted of three parts, a rigid plate that moves vertically at the top, a honeycomb in the middle, and a rigid plate with all degrees of freedom restrained at the bottom to simulate actual compression tests. In simulating the compression behavior of the specimens at room temperature, PLA plastic was represented as elastic-perfectly plastic material. The 3D models were developed using linear hexahedral element (C3D8R) with reduced integration and hourglass control. Global mesh size was set to 0.5 mm, ensuring that each wall thickness accommodates at least two elements. The coupling point was established at the geometric center of the upper rigid plate to apply velocity loads. Considering that it is very time-consuming to simulate a dynamic case with actual compression speed numerically, the current simulation speed was set to 200 mm/s. The loading condition is considered to be quasi-static when the kinetic energy keeps lower than 5–10 % of the total energy[53]. General contact setting was performed on the model, and the tangential friction coefficient was 0.2. Convergence tests were conducted to check the validity of the numerical simulation. The post-processing process outputted the load–displacement curve of the coupling point for comparing with the experimental results.

3. Results and discussions

3.1. Mechanical behavior

3.1.1. Deformation modes

The compression behavior of three representative honeycombs was selected to understand the deformation at increasing strain levels during displacement-controlled uniaxial compression tests. Fig. 4 depicts the comparison of compression processes, the corresponding stress–strain curves, and energy absorption efficiency curves for quasi-static compression of honeycomb structures with different cell configurations. Fig. 5 compares the experimental and simulated shapes in the compressed state. Here, stress $\sigma = F/(L^*W)$, strain $\varepsilon = d/H$. The traditional accordion honeycomb has a typical compression process, as shown in Fig. 4(a), including the initial elastic deformation stage, the plateau stress stage, and the densification stage[9,44]. Before reaching the initial peak, the cell walls in contact with the top rigid plate undergo bending deformation, and the compressive load increases rapidly. As the compressive displacement increases, the inclined cell walls at the top and bottom slide against the smooth steel plate, and the cell walls gradually adhere to the plate. During the plateau stress stage, the inclined cell walls rotate at the node intersecting the horizontal cell walls, as shown in Fig. 5(a). The rotation direction is randomly indeterminate. The inclined cell walls collapse sideways and contact with the horizontal wall, while other connected inclined walls buckle. The simulation and experiment show consistent compression behavior.

Fig. 4(b) shows the compressive behavior of the completely flipped honeycomb with a 15° flip angle. The deformation mode of CF15-4–1 is the same as the traditional accordion honeycomb structure in the elastic deformation stage. However, brittle fracture of the honeycomb cell walls occurs when the force exceeds a critical value, resulting in a dramatic load drop. The simulation process is slightly different from the experimental result due to the brittle fracture property of the material is not

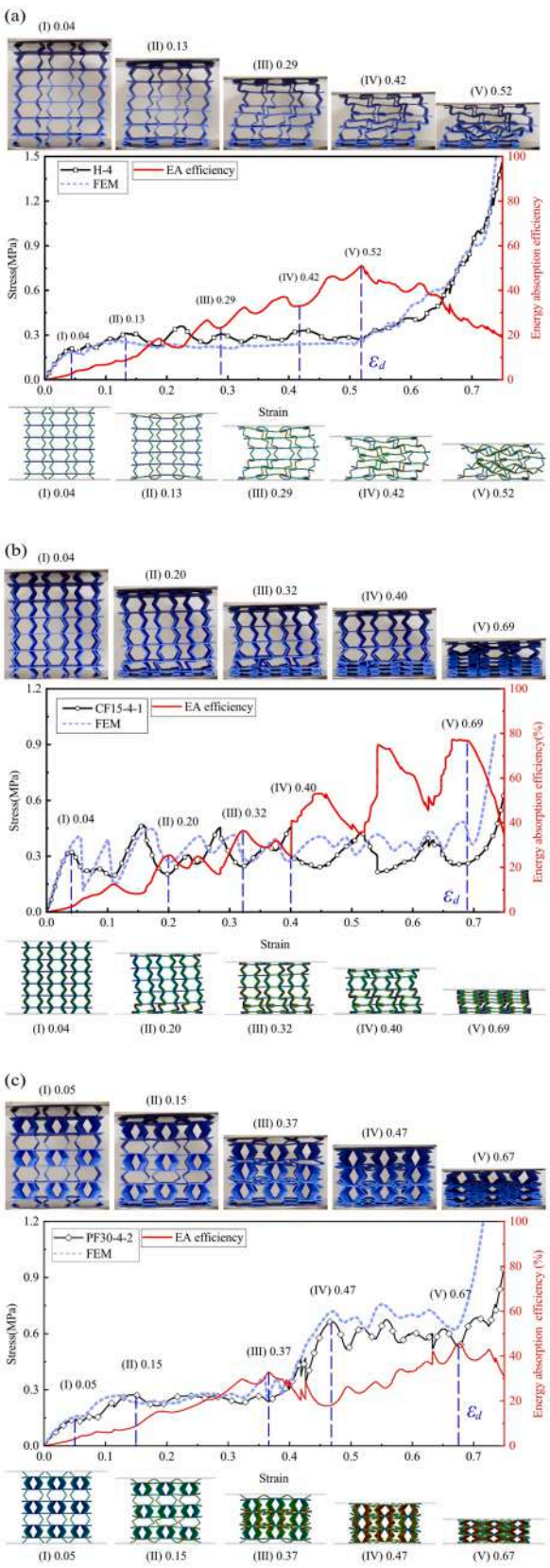

Fig. 4. Compressive deformation behaviors of honeycombs and consistency comparison between experimental test and simulation: (a) H-4, (b) CF15-4–1, and (c) PF30-4–2.

considered in the FE model. The failure modes caused by stress concentration occur in the test, as shown in Fig. 5b, including brittle fracture at the intersection of inclined and horizontal walls, fracture at the connection of inclined walls, and cracking along the symmetry plane, cannot be simulated by FE models. These phenomena are reflected in Fig. 4(b) by the sudden decrease of stress in the experimental stress–-strain curve. It is worth stating that stress output by the simulation process also drops suddenly. This can be explained by the fact that the yielding of one honeycomb layer releases the internal force of other not failed layers when the load increases beyond the material yield limit. The honeycomb structure gradually collapses as the downward displacement continues. Peaks and valleys appear when each cell level is crushed, and the peaks are higher than the initial peak. Compared with the classical hexagonal honeycomb compression process, the honeycomb cell walls yield and collapse plastically with increasing strain, with the difference that the hexagonal honeycomb exhibits an oblique line band and an ''X'' shape band[44], while the honeycombs with varying cross section collapse layer by layer.

The compression behavior of the PF honeycomb exhibits apparent differences, as shown in Fig. 4(c). The deformation process is divided into four stages. The initial process is the elastic deformation stage dominated by bending deformation, followed by the compression of the cell wall layer without flipping. When the energy absorption efficiency curve reaches the first peak, marking that the PF honeycomb starts partially densified. Next, flipped cell walls are compressed during the second plateau stage, resulting in plateau stress close to twice the previous stage. Finally, all cell walls of PF honeycomb contact each other, and the energy absorption efficiency curve reaches the second peak, indicating that the honeycomb enters the overall densification stage. The first plateau stage is relatively stable, while the latter has a larger oscillation amplitude caused by the cracking at the symmetry plane and the cell wall fracture. Therefore, the deformation sequence can be controlled by designing the position where the cell walls flipped.

As shown in Fig. 4, the trend of the curves represented by the experimental and simulation results is consistent. Especially the two curves almost coincide before reaching the initial peak. The FE simulation curve is smoother than the experiment because the fracture and crush that occurred during the experimental tests are not considered in the simulation. The experimental compression process and simulation are almost identical, with a slight difference shown in Fig. 4(b). In general, the simulation results can be considered reliable.

3.1.2. *The effect of flip angle*

The flip angle is an essential parameter of the variable cross-section honeycomb structures. The introduction of the flip angle brings changes in the compressive properties of the honeycomb structure. Fig. 6 plots the compressive stress–strain curves of conventional accordion honeycombs and honeycombs with flip angles of 15° and 30°. The traditional accordion honeycomb could be considered a case where the flip angle is zero. Fig. 6(a) and Fig. 6(b) show the CF honeycomb compressive stress–strain curves of the 2-layer and the 4-layer backward symmetric mode, respectively. The initial stress peak in both figures increases significantly with the flip angle, and the slope of the curve also raises at the initial elastic stage. It can be considered that the introduced flip angle enhances the bearing performance of the honeycomb within a certain range, and the larger the angle, the stronger the enhancement effect, apart from the CF30-2–2 specimen, which produces out-of-plane buckling with increasing compressive strain. This phenomenon could be explained by the inconsistency of deformation along the width direction when compressing the honeycomb cell walls. Due to the constraint of the symmetry plane, the part farther from the symmetry plane contacting the indenter is more susceptible to deform, resulting in out-of-plane buckling deformation. In addition, as the flip angle increases, the stress oscillation amplitude is greater after a linear growth with the strain. Especially for CF30-4–2, the stress dropped instantly by 0.4 MPa caused by the crushing of the whole honeycomb cell level, which does

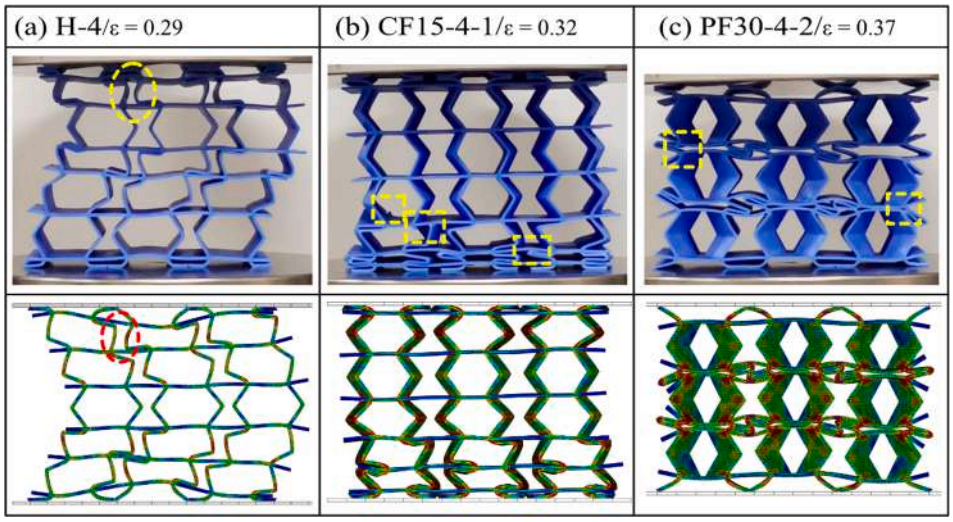

Fig. 5. Deformed shape of the structures under compression: FE simulated and experimental: (a) H-4, (b) CF15-4–1, and (c) PF30-4–2.

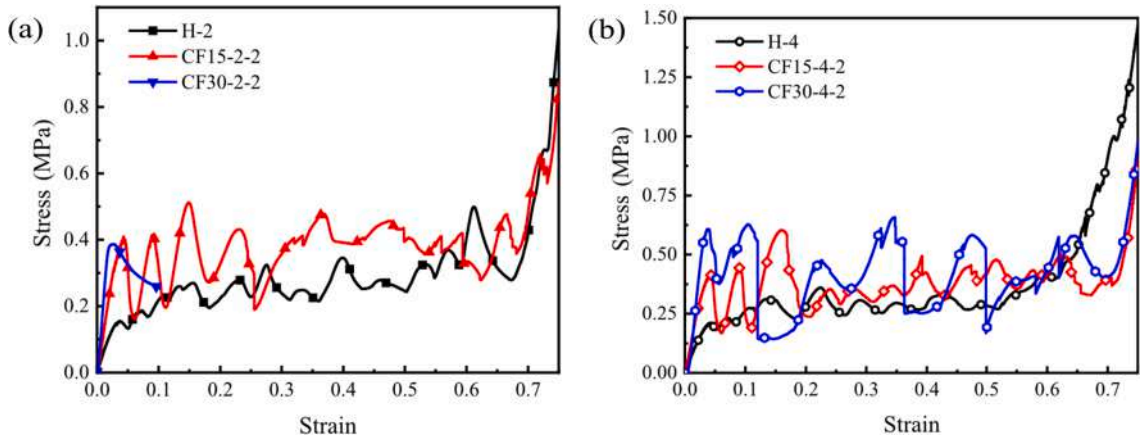

Fig. 6. Compression properties of CF honeycombs with various flipped angles: (a) 2 times and (b) 4 times the cell width.

not occur in traditional accordion honeycombs.

Fig. 7 shows the effect of flip angle on compression modulus and specific modulus. Specific modulus is the ratio of compression modulus to relative density. The compression modulus and specific modulus of all tested honeycomb specimens are summarized in Table 2. It is clear that the compression modulus increases with the flip angle. The compression modulus is over twice the conventional honeycomb when the flip angle is 15°, and more than four times when the flip angle is 30°. The

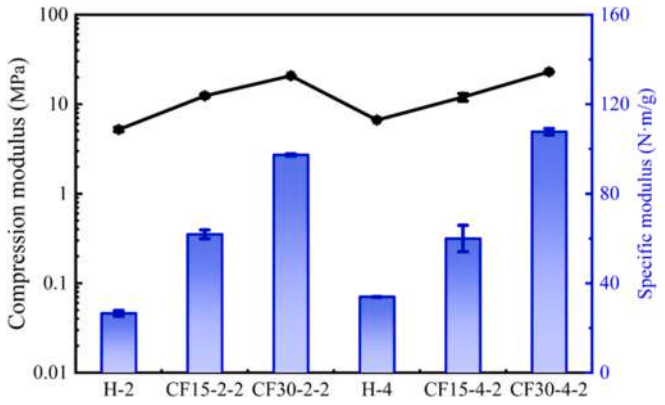

Fig. 7. Effect of flip angle on compressive and specific modulus.

Table 2
Compression properties of 3D printed accordion honeycomb and honeycombs with varying cross section.

Structure	Compression modulus (MPa)	Specific modulus (N·m/g)
H-2	5.82 ± 0.25	26.57 ± 1.26
CF15-2–1	11.03 ± 0.71	55.09 ± 3.52
CF15-2–2	12.39 ± 0.39	61.86 ± 1.95
CF30-2–1	17.53 ± 0.88	82.05 ± 4.11
CF30-2–2	20.81 ± 0.11	97.36 ± 0.50
CF15-3	11.35 ± 1.02	56.67 ± 5.11
CF30-3	18.17 ± 0.42	85.03 ± 0.20
H-4	6.03 ± 0.02	33.91 ± 0.11
CF15-4–1	10.12 ± 0.08	50.50 ± 0.39
CF15-4–2	12.02 ± 1.18	60.00 ± 5.88
CF30-4–1	20.13 ± 0.63	94.18 ± 2.95
CF30-4–2	25.58 ± 0.31	107.73 ± 1.46
PF30-4–2	3.84 ± 0.06	18.75 ± 0.29
RF30-4	12.59 ± 0.26	58.93 ± 1.22
CW-4–2	26.89 ± 0.23	130.10 ± 1.09
RW-4	13.45 ± 0.40	65.07 ± 1.91

compression modulus of the traditional accordion honeycomb structure with two-layer and four-layer unit cell widths are 5.82 MPa and 6.03 MPa, respectively. In comparison, the maximum modulus increases to 25.58 MPa when the flip angle is 30°. Therefore, it can be concluded that the variable cross-section design in the width direction enhanced the in-

plane bearing capability of the traditional accordion honeycomb.

3.1.3. The effect of symmetry mode

The changed cross-section in the width direction of a unit cell makes the honeycomb structures different in the forward and backward symmetry modes. The compressive behaviors of several specimens with the same flipped angle are compared. Fig. 8(a) and Fig. 8(b) display the compressive stress–strain curves of honeycombs with different symmetry modes at 15° and 30° flip angles, respectively. When the flip angle is 15°, as shown in Fig. 8(a), the slopes of the five types of specimens at the initial elastic stage almost coincide, but the initial peaks are pretty different. Among them, the initial stress peak values of the backward symmetric mode (CF15-2–2, CF15-4–2) are higher than that of the forward (CF15-2–1, CF15-4–1). However, the cell walls of the former are more prone to brittle fracture and easier to crack at the symmetrical plane. Fig. 8(b) shows a similar trend when the flip angle is 30°. The multiplication of width motivates the significant growth of the initial stress peak and rapid stress decline. Fig. 9 compares the calculated compression modulus and specific modulus, and corresponding results are listed in Table 2. The backward symmetry modes have larger compression moduli than the front symmetry style at flip angles of 15° and 30°. By comparison, it is found that the bearing capability of the backward symmetric modes was better than that of the ahead symmetry styles, but the former's stabilities are worse than the latter.

3.1.4. The effect of unit cell topology

Fig. 10 display the in-plane compressive stress–strain curves of honeycomb structures with diverse unit cell topologies. The compression modulus and specific modulus corresponding to the honeycombs are listed in Table 2 and shown in Fig. 11. Compared with the traditional accordion honeycomb structure, the variable cross-section honeycombs with different unit cell configurations have significantly improved mechanical performance in the initial elastic stage, with the PF30-4–2 exception. The initial stress peak and slope of PF30-4–2 honeycomb are smaller than conventional honeycomb. The CW-4–2 honeycomb and the PF30-4 honeycomb have the maximum and minimum compressive moduli of 26.89 MPa and 3.85 MPa, respectively, corresponding to the maximum and minimum specific moduli of 130.10 N·m/g and 18.75 N·m/g. In addition, the compression modulus and initial stress peak value of RF30-4 and RW-4 are slighter than CF30-4–2 and CW-4–2 in the initial elastic stage due to the deformability inconsistency of the upper and lower inclined walls. The inclined walls with forwarding symmetry mode have the weaker load-bearing capability and are compressed first, determining the stress peak at the initial elastic stage. This characteristic is consistent with the outcome studied in Section 3.1.2 that the honeycombs' load-bearing performance with backward symmetry mode is superior to the forward symmetry way. The CW-4–2 honeycomb has higher initial peak stress and more massive stress decline than the CF30-4–2 honeycomb due to the improved stress concentration. The cell walls are more uniformly compressed and cannot guide where the fracture occurred, resulting in a sharp decrease after the entire layer collapses. In order to avoid the sudden decline of stress, raw material with better ductility can be utilized to achieve better compression performance. Furthermore, the variable stiffness properties, i.e., the stiffness and deformability as a function of ambient temperature, could be used to improve compression behavior.

3.2. Energy absorption

The energy absorption performance of honeycomb structures is usually evaluated by densification strain, total energy absorption (EA), specific energy absorption (SEA), and crushing force efficiency (CFE). The densification strain ε_d, referring to the strain at the onset of densification stage during the compression process, can be solved by the EA efficiency method[8]. The EA efficiency $\eta(\varepsilon)$ is defined as the ratio of the area of the stress–strain curve to the stress $\sigma(\varepsilon)$, and the strain ε corresponding to the maximum EA efficiency is the densification strain. The calculation formulas are expressed as follows:

$$\eta(\varepsilon) = \frac{\int_0^{\varepsilon} \sigma(\varepsilon)d\varepsilon}{\sigma(\varepsilon)}, 0 \le \varepsilon \le 1 \tag{3}$$

$$\left.\frac{d\eta(\varepsilon)}{d\varepsilon}\right|_{\varepsilon=\varepsilon_d} = 0, 0 \le \varepsilon_d \le 1 \tag{4}$$

The EA efficiency curve has a maximum because the increase of absorbed energy is lower than the corresponding stress increase when densification state starts[54]. It should be noted that, due to the sudden load drop caused by the collapse of the honeycomb level, the EA efficiency-strain curve will have a sharp point. Therefore, when calculating the densification strain in this case, the strain corresponding to the local maximum stress at the end is regarded as the densification strain. EA is obtained from the area of the load–displacement curve before entering the densification stage, expressed by the equation (5), where δ_d is the compressive displacement at the beginning of the densification, and $F(\delta)$ is the compressive load. SEA is the ratio of EA to mass m, one of the critical indicators to characterize energy absorption performance.

$$\mathrm{EA} = \int_0^{\delta_d} F(\delta)d\delta \tag{5}$$

$$\mathrm{SEA} = \frac{\mathrm{EA}}{m} \tag{6}$$

CFE is defined as the ratio of the average crushing force to the initial peak force (IPF), a crashworthiness parameter that expresses the

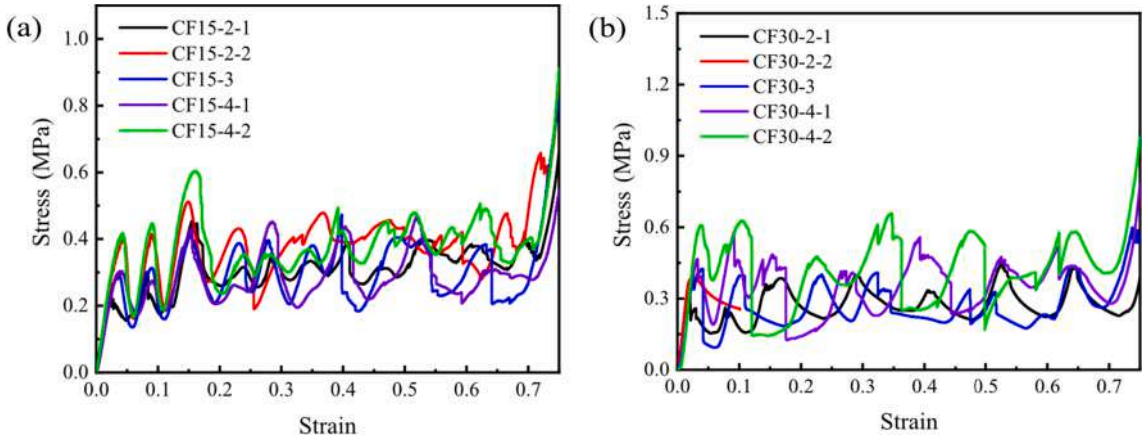

Fig. 8. Compression properties of CF honeycombs with different symmetry modes: (a) 15° flip angle and (b) 30° flip angle.

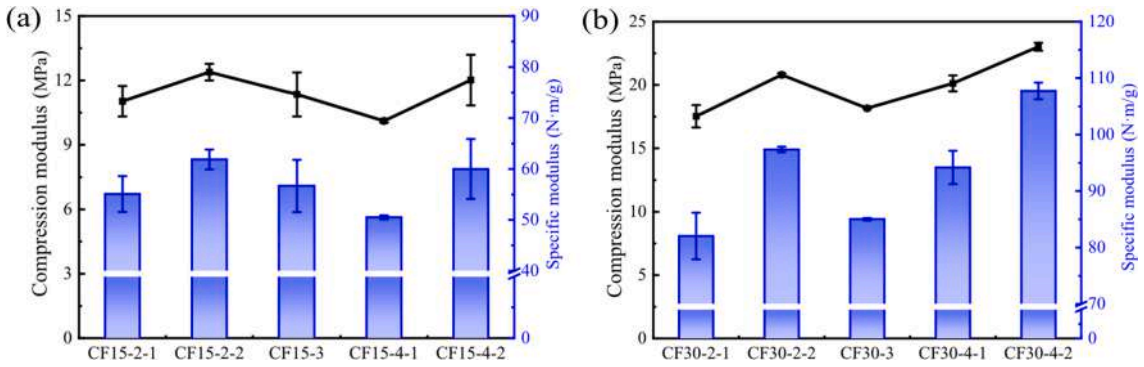

Fig. 9. Effect of symmetry mode on compression and specific modulus. (a) 15° flip angle and (b) 30° flip angle.

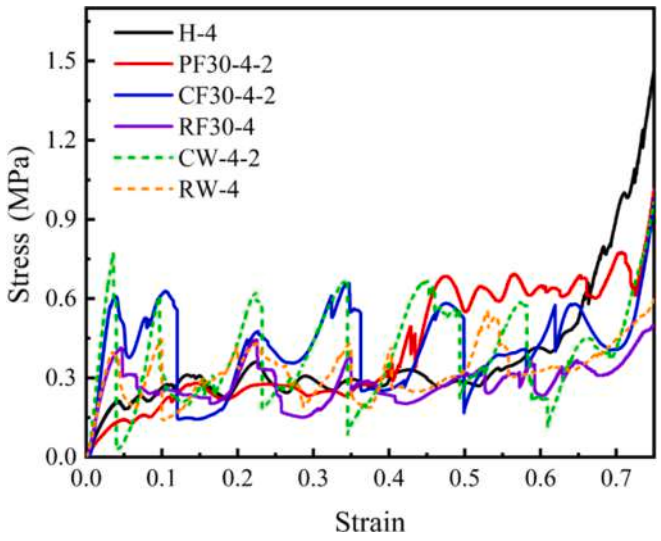

Fig. 10. Compression properties of variable cross-section honeycombs with different topologies.

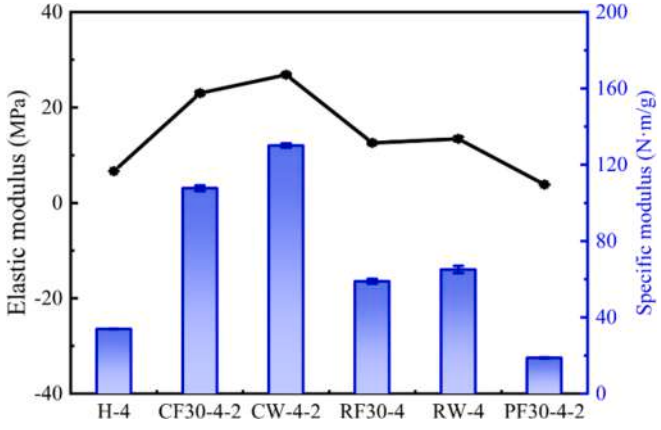

Fig. 11. Effect of unit cell topology on compressive and specific modulus.

uniformity of compressive force. It determines whether the compression failure is progressive or fatal. Fatal failures are characterized by high IPF, small average crushing force, and less CFE.

$$\mathrm{CFE} = \frac{\mathrm{EA}}{\delta_d \cdot \mathrm{IPF}} \tag{7}$$

Fig. 12 presents the energy absorption characteristics of the designed variable cross-section honeycomb structures under in-plane compressive loading. As shown in Fig. 12(a), the honeycomb specimens with four times cell width have a larger bearing area, so their EA is significantly higher than those with three or two times cell width. The EA of designed variable cross-section honeycomb structures is greater than the traditional accordion honeycomb structure at the same width, so is the SEA. For example, the EA of classic accordion honeycomb at 20 mm width is 22.7 J, while the CF15-2–2 honeycomb absorbs 41.2 J, nearly-two times that of the former. The EA of the accordion honeycomb with 40 mm width is 51.8 J, while the EA of CF30-4–2 is 85.4 J. The SEA range of the honeycomb structures is 0.77 kJ/kg – 1.36 kJ/kg, and the minimum and maximum values correspond to the accordion honeycomb with 20 mm width and CF15-4–2 honeycomb.

Fig. 12(b) compares crashworthiness parameters between traditional accordion honeycombs and variable cross-section honeycombs. At the same flip angle, the larger the honeycomb width, the greater the IPF, and the smaller the CFE. For example, the IPF of CF15-2–2 and CF15-4–2 honeycombs is 0.69 kN and 1.46 kN, but the CFE is 91 % and 84 %, respectively. Except for the PF30-4 honeycomb, other honeycombs with 40 mm width have high IPF while the compressive failure is fatal, so the CFE is relatively lower, around 60 %. The compression failure modes of the traditional accordion honeycomb structure and PF30-4 are progressive, and the CFE exceeds 100 %. Especially for PF30-4–2, the CFE reaches 270 %. The SEA of PF30-4–2 honeycomb is 1.35 kJ/kg, exhibiting excellent energy absorption performance though the IPF proves relatively low.

In order to fully reflect the effect of the variable cross-section design on energy absorption performance, this work is compared with other familiar cellular configurations. The comparison of honeycomb structures based on polymer materials is performed, and the distribution of in-plane SEA is plotted in Fig. 13. It can be seen that the SEA of the variable section honeycomb structure is similar to the re-entrant chiral auxetic (RCA) structure studied in reference[19], which is manufactured from nylon 12, and the auxetic honeycomb material in reference[48] fabricated by Kevlar fiber reinforced PLA. However, the density of the honeycombs in the present work is lower than both. It means that the three have comparable energy absorbing capability, but the variable-section honeycomb structures have lighter weight. Compared to SMP re-entrant honeycomb[12], ABS hexagonal honeycomb and hybrid honeycomb[23], nylon 2200 hexagonal and re-entrant hybrid honeycomb[26], nylon 12 hexagonal honeycomb[44], and perforated structures with short carbon fiber reinforced nylon[46], variable cross-section honeycomb structures have the highest SEA showing apparent superiority. Compared with the hexagonal honeycomb fabricated by the aluminum alloy (AlSi10Mg) [55] and origami-inspired honeycomb manufactured by stainless steel 304L[36], the in-plane SEA of the proposed variable-section honeycomb structure is slightly lower, but the honeycomb mass is much smaller. The variable-section honeycomb has the same level of energy absorption capacity as hierarchical honeycombs prepared by the aluminum alloy AA3030-H19[56], while the former has a greater mass. However, the in-plane SEA of the present

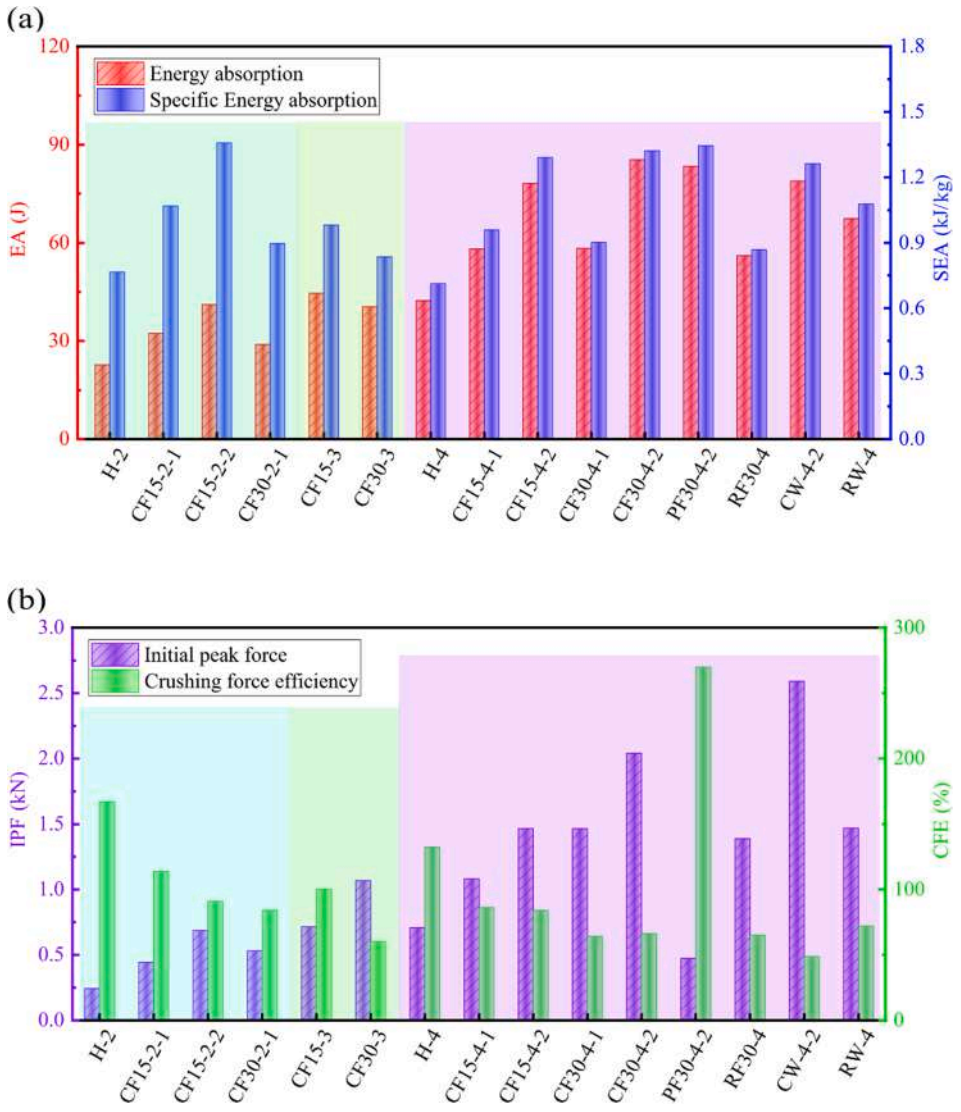

Fig. 12. Energy absorption characteristics of variable cross-section honeycombs: (a) EA and SEA; (b) IPF and CFE.

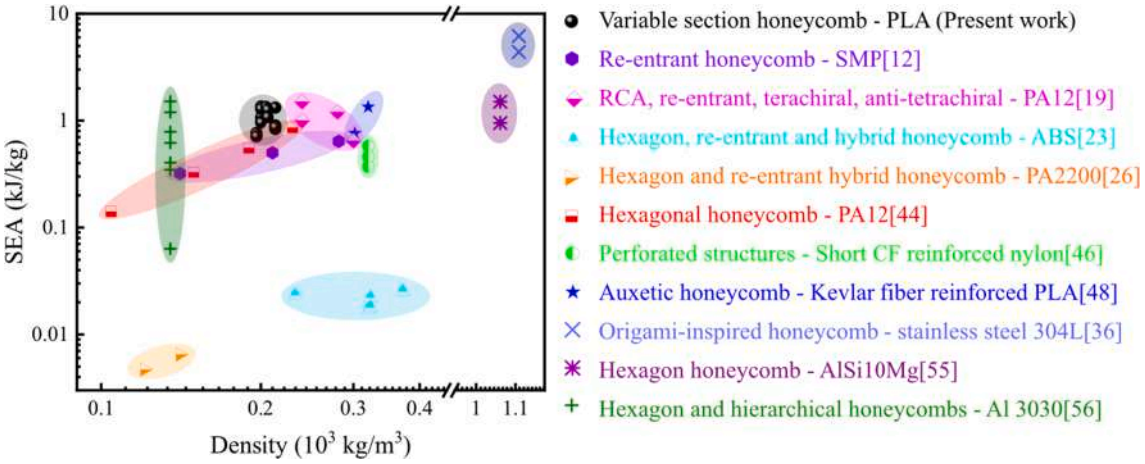

Fig. 13. SEA comparison between variable cross-section honeycombs and competitive cellular topologies.

work is much greater than that of the regular honeycomb (the green cross symbol at the bottom).

3.3. Isothermal compression behavior

The parent material converts from a rigid state at low temperature to a flexible state at high temperature. The compressive properties and energy absorption characteristics of the honeycombs are tunable by controlling the temperature. Therefore, the variable cross-section honeycomb structures' isothermal compressive behavior versus temperature is investigated. The isothermal compressive tests are characterized at 40 °C, 45 °C, and 50 °C. The load–displacement curves are plotted in Fig. 14. The load-bearing performance of the traditional accordion honeycomb structure under different temperatures is the lowest, including the IPF and compression modulus, and the load oscillation is the smallest in the plateau stress stage. The CF honeycombs present the best load-bearing performance, followed by RF and RW honeycombs. As the temperature increases, the load-bearing capability of the honeycomb decreases, and the force–displacement curve becomes smooth.

Fig. 15 displays a specific modulus nephogram for demonstrating the effect of temperature on the compression modulus. Apparently, the growing ambient temperature reduces the specific compression modulus. Compared to the classical accordion honeycomb, the specific modulus of the variable cross-section honeycomb has been improved to a certain extent at experimental temperatures. It is worth noting that the specific modulus of the designed honeycomb structures at higher temperatures is greater than that of the traditional accordion honeycomb at room temperature, proving that the variable cross-section design to enhance mechanical properties is effective.

The comparison of the energy absorption performance between accordion honeycomb and designed variable cross-section honeycomb at different temperatures is shown in Fig. 16. The temperature has a negligible impact on the densification displacement, but the falling load leads to a decrease in EA. Nonetheless, the histogram in Fig. 16(d) shows that the EA of variable cross-section honeycomb structures at 40 and 45 ℃, and the EA of CF30-4–2 honeycomb at 50 ℃, are higher than the EA of traditional accordion honeycomb at 25 ℃. The CF30-4–2 honeycomb is the most noticeable structure, whose EA at 40 °C is higher than the energy absorbed during the compression process at room temperature. This phenomenon appears due to the load keeping relatively low when the cell walls are collapsed at room temperature and experiences a long compression displacement before the force rises again. The fractured layer is compacted then other cell wall levels begin to compress. In contrast, the parent material has good ductility at 40 ℃ and would not generate cell wall collapse during compression. The cell walls yield under downward compression, so the load decreases until the walls contact. The variable stiffness characteristic of PLA can improve the energy absorption properties to some extent of the novel honeycomb structures. In addition, metals with better ductility can be used instead of polymers to enhance the compressive properties and energy absorption properties of variable cross-section honeycomb structures.

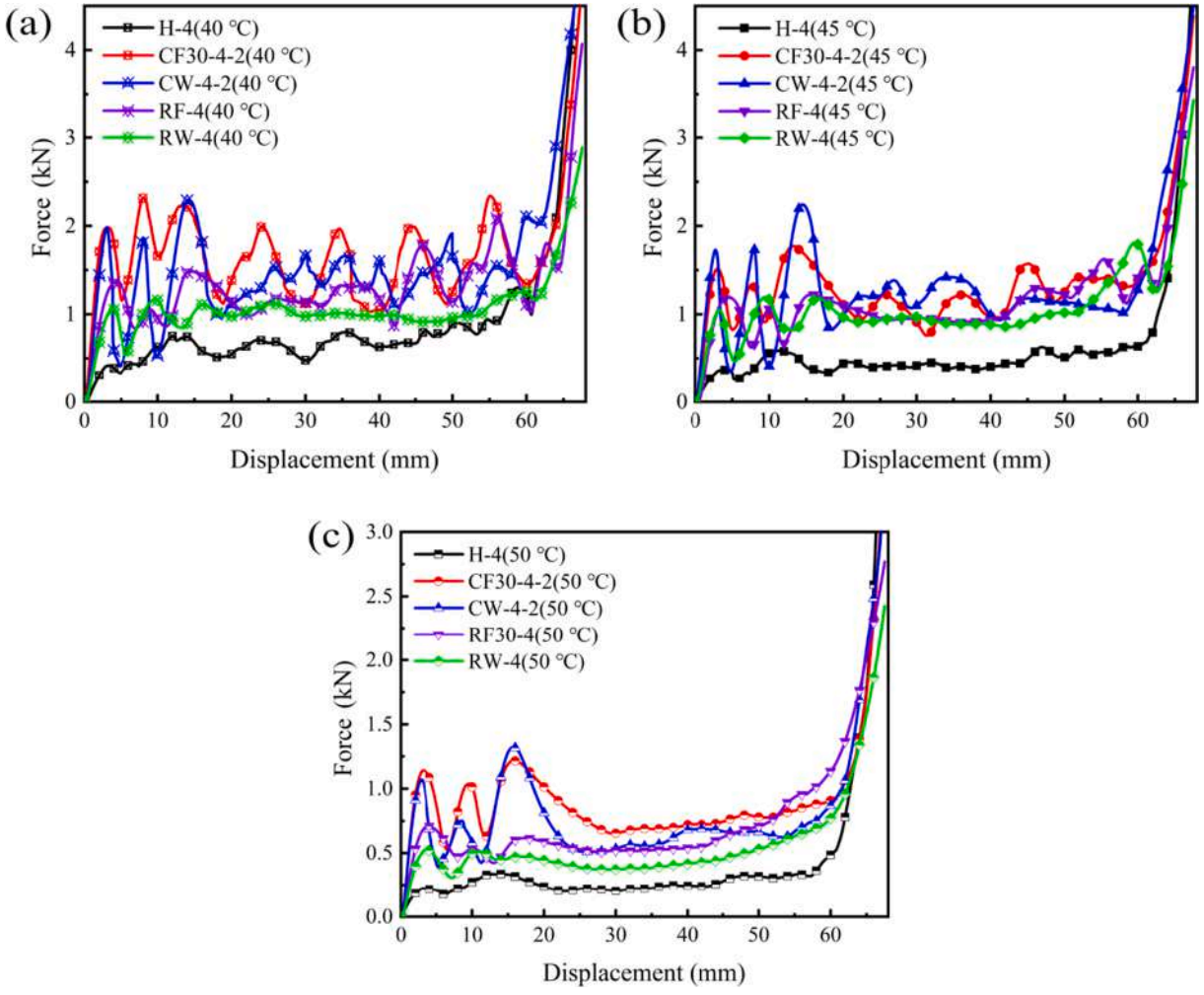

Fig. 14. Comparison of load–displacement curves at different temperatures: (a) 40 °C, (b) 45 °C, and (c) 50 °C.

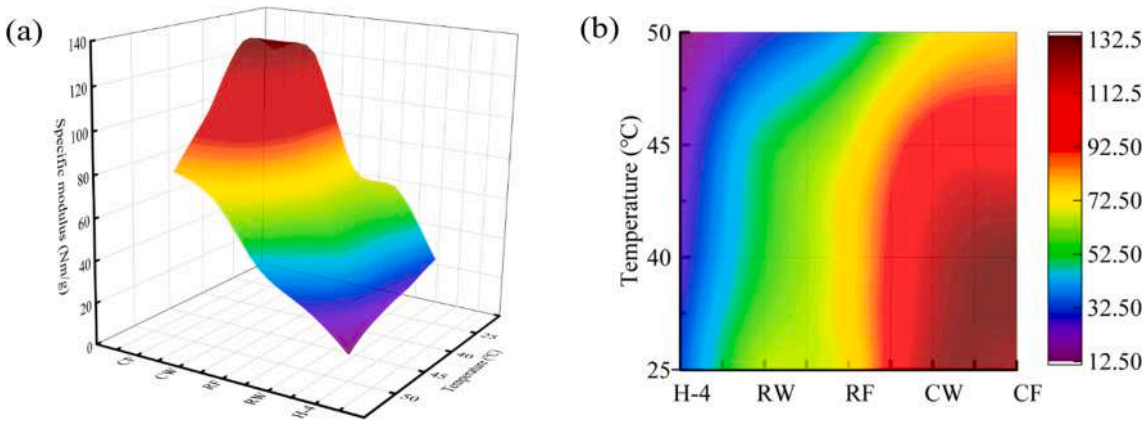

Fig. 15. Specific modulus nephogram with temperature: (a) 3D surface graph and (b) mapping surface graph.

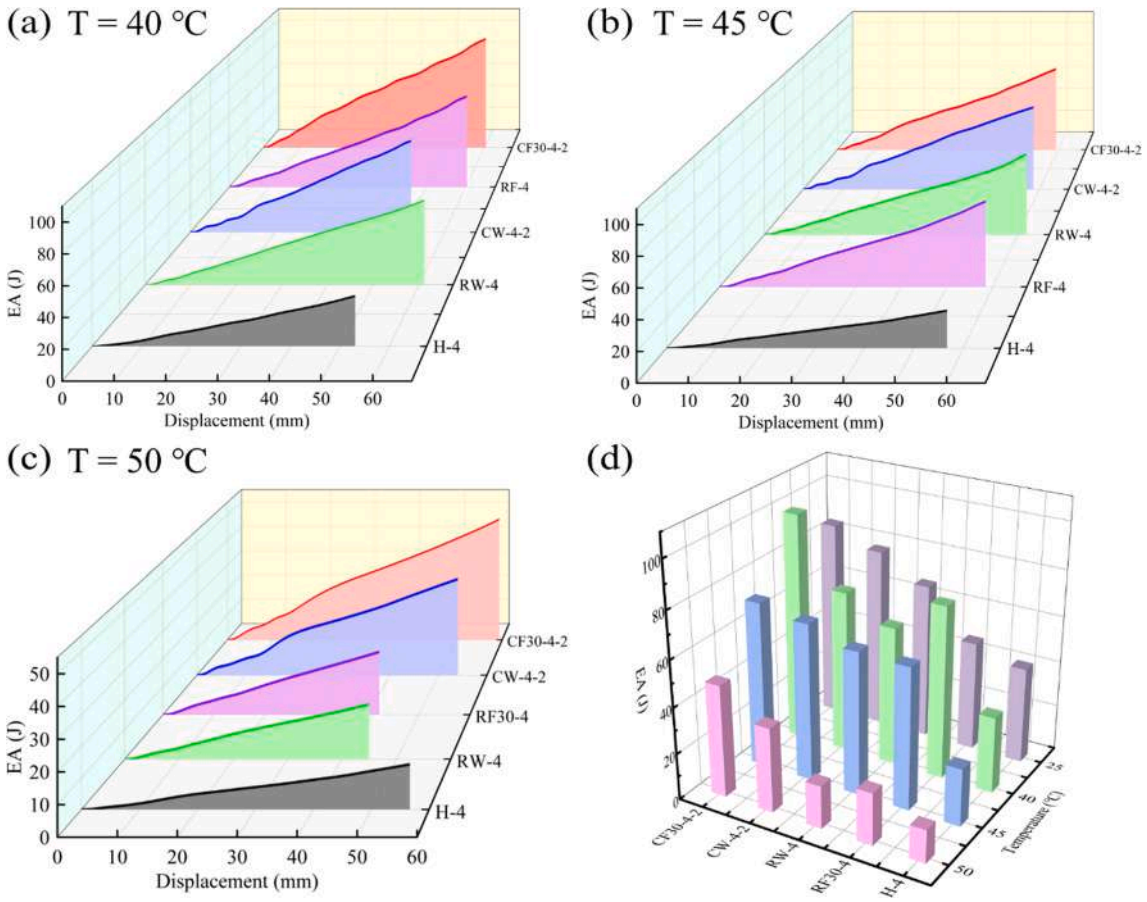

Fig. 16. EA performance of traditional accordion honeycomb and variable cross-section honeycombs: EA-displacement curve at (a) 40 °C, (b) 45 °C, and (c) 50 °C; (d) EA comparison of honeycombs.

4. Conclusions

A novel cellular structure with varying cross-sectional dimensions was proposed to enhance mechanical properties and energy absorption capability. Quasi-static compression tests were applied to characterize compression behavior and energy absorption. The effects of flip angle, symmetry mode, and unit cell configuration on the load-bearing capability and energy absorption were compared by experimental tests. The results show that both the compression modulus and the specific energy absorption have been improved with increasing flip angles. The compression modulus and specific energy absorption of the traditional accordion honeycomb with a width of 40 mm were 6.03 MPa and 0.72 kJ/kg, respectively, while that of the CF30-4–2 honeycomb increased to 25.58 MPa and 1.32 kJ/kg. Although the compression modulus of PF30-4–2 honeycomb is the smallest of 3.85 MPa, the specific energy absorption reaches 1.35 kJ/kg. The compression sequence could be controlled by designing unit cell configurations. The compression process simulated by the FE model was in good agreement with the experiments. Compared with the traditional accordion honeycomb structure, the stress–strain curves of the variable cross-section honeycombs oscillated more intensely because of the brittle fracture of the cell walls. Isothermal compression experiments were performed considering

the parent material's variable stiffness. Although the increasing temperature declined the compressive stress of the variable cross-section honeycombs, the sudden stress drop was alleviated. Furthermore, the EA of the CF30-4–2 honeycomb at 40 °C was higher than that at room temperature. The EA of most variable-section honeycomb structures at high temperatures was greater than that of traditional accordion honeycombs at room temperature. In summary, honeycomb structures with varying cross-section dimensions were proposed. The designed honeycombs, fabricated by 3D printing technology with PLA material, were experimentally verified the significant improvement of the accordion honeycombs' load bearing and energy absorbing properties.

CRediT authorship contribution statement

Ting Li: Conceptualization, Investigation, Visualization, Writing – original draft, Writing – review & editing. **Jian Sun:** Conceptualization, Supervision, Writing – review & editing. **Jinsong Leng:** Visualization, Writing – review & editing. **Yanju Liu:** Conceptualization, Methodology, Supervision, Writing – review & editing.

Declaration of Competing Interest

The authors declare that they have no known competing financial interests or personal relationships that could have appeared to influence the work reported in this paper.

Data availability

Data will be made available on request.

Acknowledgment

This work is supported by the National Natural Science Foundation of China (Grant No 12172106) and the Fundamental Research Funds for the Central Universities (Grant No. HIT.OCEF.2021009).

References

[1] Gibson LJ, Ashby MF. Cellular solids: structure and properties. Cambridge, UK: Cambridge Univ. Press; 1999.
[2] Zhang Q, Yang X, Li P, Huang G, Feng S, Shen C, et al. Bioinspired engineering of honeycomb structure – Using nature to inspire human innovation. Prog Mater Sci 2015;74:332–400.
[3] Nunes JP, Silva JF. Sandwiched composites in aerospace engineering. Advanced Composite Materials for. Aerosp Eng 2016:129–74.
[4] Peng Y, Deng W, Xu P, Yao S. Study on the collision performance of a composite energy-absorbing structure for subway vehicles. Thin-Walled Struct 2015;94:663–72.
[5] Zhou H, Xu P, Xie S. Composite energy-absorbing structures combining thin-walled metal and honeycomb structures. Proc Inst Mech Eng Pt F: J Rail Rapid Transit 2016;231(4):394–405.
[6] Shin KB, Lee JY, Cho SH. An experimental study of low-velocity impact responses of sandwich panels for Korean low floor bus. Compos Struct 2008;84(3):228–40.
[7] Palomba G, Epasto G, Crupi V. Lightweight sandwich structures for marine applications: a review. Mech Adv Mater Struct 2022;29(26):4839–64.
[8] Li QM, Magkiriadis I, Harrigan JJ. Compressive strain at the onset of densification of cellular solids. J Cell Plast 2016;42(5):371–92.
[9] Ashby MF. The properties of foams and lattices. Phil Trans R Soc A 1838;2006(364):15–30.
[10] Dong Z, Li Y, Zhao T, Wu W, Xiao D, Liang J. Experimental and numerical studies on the compressive mechanical properties of the metallic auxetic reentrant honeycomb. Mater Des 2019;182:108036.
[11] Harkati A, Boutagouga D, Harkati E, Bezazi A, Scarpa F, Ouisse M. In-plane elastic constants of a new curved cell walls honeycomb concept. Thin-Walled Struct 2020;149:106613.
[12] Ji L, Hu W, Tao R, Liao B, Wan Z, Wu W, et al. Compression behavior of the 4D printed reentrant honeycomb: experiment and finite element analysis. Smart Mater Struct 2020;29(11):115016.
[13] Qu Y, Wang D, Zhang H. The equivalent method of double V-wing honeycombs on the in-plane dynamic impact. J Reinf Plast Compos 2021;40(15–16):577–93.
[14] Guo M-F, Yang H, Ma Li. Design and analysis of 2D double-U auxetic honeycombs. Thin-Walled Struct 2020;155:106915.
[15] Wei L, Zhao X, Yu Q, Zhang W, Zhu G. In-plane compression behaviors of the auxetic star honeycomb: Experimental and numerical simulation. Aerosp Sci Technol 2021;115:106797.
[16] Wei L, Zhao X, Yu Q, Zhu G. Quasi-static axial compressive properties and energy absorption of star-triangular auxetic honeycomb. Compos Struct 2021;267:113850.
[17] Feng G, Li S, Xiao L, Song W. Energy absorption performance of honeycombs with curved cell walls under quasi-static compression. Int J Mech Sci 2021;210:106746.
[18] Günaydın K, Eren Z, Kazancı Z, Scarpa F, Grande AM, Türkmen HS. In-plane compression behavior of anti-tetrachiral and re-entrant lattices. Smart Mater Struct 2019;28(11):115028.
[19] Alomarah A, Masood SH, Sbarski I, Faisal B, Gao Z, Ruan D. Compressive properties of 3D printed auxetic structures: experimental and numerical studies. Virtual Phys Prototyp 2019;15(1):1–21.
[20] Alomarah A, Ruan D, Masood S, Gao Z. Compressive properties of a novel additively manufactured 3D auxetic structure. Smart Mater Struct 2019;28(8):085019.
[21] Peng X-L, Bargmann S. A novel hybrid-honeycomb structure: Enhanced stiffness, tunable auxeticity and negative thermal expansion. Int J Mech Sci 2021;190:106021.
[22] Xu M, Liu D, Wang P, Zhang Z, Jia H, Lei H, et al. In-plane compression behavior of hybrid honeycomb metastructures: Theoretical and experimental studies. Aerosp Sci Technol 2020;106:106081.
[23] Ingrole A, Hao A, Liang R. Design and modeling of auxetic and hybrid honeycomb structures for in-plane property enhancement. Mater Des 2017;117:72–83.
[24] Logakannan KP, Ramachandran V, Rengaswamy J, Gao Z, Ruan D. Quasi-static and dynamic compression behaviors of a novel auxetic structure. Compos Struct 2020;254:112853.
[25] Alomarah A, Xu S, Masood SH, Ruan D. Dynamic performance of auxetic structures: experiments and simulation. Smart Mater Struct 2020;29(5):055031.
[26] Xu M, Xu Z, Zhang Z, Lei H, Bai Y, Fang D. Mechanical properties and energy absorption capability of AuxHex structure under in-plane compression: Theoretical and experimental studies. Int J Mech Sci 2019;159:43–57.
[27] Farrokhabadi A, Veisi H, Gharehbaghi H, Montesano J, Behravesh AH, Hedayati SK. Investigation of the energy absorption capacity of foam-filled 3D-printed glass fiber reinforced thermoplastic auxetic honeycomb structures. Mech Adv Mater Struct 2022:1–12.
[28] Farrokhabadi A, Mahdi Ashrafian M, Behravesh AH, Kaveh Hedayati S. Assessment of fiber-reinforcement and foam-filling in the directional energy absorption performance of a 3D printed accordion cellular structure. Compos Struct 2022;297:115945.
[29] Zhang Y, Lin Y, Li Y, Li X. 3D printed self-similar AlSi10Mg alloy hierarchical honeycomb architectures under in-plane large deformation. Thin-Walled Struct 2021;164:107795.
[30] Liu Hu, Zhang ET, Ng BF. In-plane dynamic crushing of a novel honeycomb with functionally graded fractal self-similarity. Compos Struct 2021;270:114106.
[31] Li S, Liu Z, Shim VPW, Guo Y, Sun Z, Li X, et al. In-plane compression of 3D-printed self-similar hierarchical honeycombs – Static and dynamic analysis. Thin-Walled Struct 2020;157:106990.
[32] Ufodike CO, Wang H, Ahmed MF, Dolzyk G, Jung S. Design and modeling of bamboo biomorphic structure for in-plane energy absorption improvement. Mater Des 2021;205:109736.
[33] Zhang P, Qi D, Xue R, Liu K, Wu W, Li Y. Mechanical design and energy absorption performances of rational gradient lattice metamaterials. Compos Struct 2021;277:114606.
[34] Vyavahare S, Teraiya S, Kumar S. Auxetic structures fabricated by material extrusion: an experimental investigation of gradient parameters. Rapid Prototyp J 2021;27(5):1041–58.
[35] Shao Y, Meng J, Ma G, Ren S, Fang L, Cao X, et al. Insight into the negative Poisson's ratio effect of the gradient auxetic reentrant honeycombs. Compos Struct 2021;274:114366.
[36] Li Q, Zhi X, Fan F. Quasi-static compressive behaviour of 3D-printed origami-inspired cellular structure: experimental, numerical and theoretical studies. Virtual Phys Prototyp 2021;17(1):69–91.
[37] Lin K, Gu D, Hu K, Yang J, Wang H, Yuan L, et al. Laser powder bed fusion of bio-inspired honeycomb structures: Effect of twist angle on compressive behaviors. Thin-Walled Struct 2021;159:107252.
[38] Ufodike CO, Ahmed MF, Dolzyk G. Additively manufactured biomorphic cellular structures inspired by wood microstructure. J Mech Behav Biomed Mater 2021;123:104729.
[39] Murphy SV, Atala A. 3D bioprinting of tissues and organs. Nat Biotechnol 2014;32(8):773–85.
[40] Ngo TD, Kashani A, Imbalzano G, Nguyen KTQ, Hui D. Additive manufacturing (3D printing): A review of materials, methods, applications and challenges. Compos B Eng 2018;143:172–96.
[41] Ligon SC, Liska R, Stampfl J, Gurr M, Mulhaupt R. Polymers for 3D Printing and Customized Additive Manufacturing. Chem Rev 2017;117(15):10212–90.
[42] González-Henríquez CM, Sarabia-Vallejos MA, Rodriguez-Hernandez J. Polymers for additive manufacturing and 4D-printing: Materials, methodologies, and biomedical applications. Prog Polym Sci 2019;94:57–116.
[43] Huang J, Chen Q, Jiang H, Zou B, Li L, Liu J, et al. A survey of design methods for material extrusion polymer 3D printing. Virtual Phys Prototyp 2020;15(2):148–62.
[44] Habib FN, Iovenitti P, Masood SH, Nikzad M. In-plane energy absorption evaluation of 3D printed polymeric honeycombs. Virtual Phys Prototyp 2017;12(2):117–31.

[45] Andrew JJ, Alhashmi H, Schiffer A, Kumar S, Deshpande VS. Energy absorption and self-sensing performance of 3D printed CF/PEEK cellular composites. Mater Des 2021;208:109863.
[46] Chen Y, He Q. 3D-printed short carbon fibre reinforced perforated structures with negative Poisson's ratios: Mechanisms and design. Compos Struct 2020;236:111859.
[47] Zeng C, Liu L, Bian W, Leng J, Liu Y. Compression behavior and energy absorption of 3D printed continuous fiber reinforced composite honeycomb structures with shape memory effects. Addit Manuf 2021;38:101842.
[48] Quan C, Han B, Hou Z, Zhang Qi, Tian X, Lu TJ. 3d printed continuous fiber reinforced composite auxetic honeycomb structures. Compos B Eng 2020;187:107858.
[49] Cheng Y, Li J, Qian X, Rudykh S. 3D printed recoverable honeycomb composites reinforced by continuous carbon fibers. Compos Struct 2021;268:113974.
[50] Barletta M, Gisario A, Mehrpouya M. 4D printing of shape memory polylactic acid (PLA) components: Investigating the role of the operational parameters in fused deposition modelling (FDM). J Manuf Process 2021;61:473–80.
[51] Liu T, Liu L, Zeng C, Liu Y, Leng J. 4D printed anisotropic structures with tailored mechanical behaviors and shape memory effects. Compos Sci Technol 2020;186:107935.
[52] Lin C, Zhang L, Liu Y, Liu L, Leng J. 4D printing of personalized shape memory polymer vascular stents with negative Poisson's ratio structure: A preliminary study. Sci China Technol Sci 2020;63(4):578–88.
[53] Esnaola A, Elguezabal B, Aurrekoetxea J, Gallego I, Ulacia I. Optimization of the semi-hexagonal geometry of a composite crush structure by finite element analysis. Compos B Eng 2016;93:56–66.
[54] Avalle M, Belingardi G, Montanini R. Characterization of polymeric structural foams under compressive impact loading by means of energy-absorption diagram. Int J Impact Eng 2001;25(5):455–72.
[55] Dou H, Ye W, Zhang D, Cheng Y, Wu C. Comparative study on in-plane compression properties of 3D printed continuous carbon fiber reinforced composite honeycomb and aluminum alloy honeycomb. Thin-Walled Struct 2022;176:109335.
[56] Yin H, Huang X, Scarpa F, Wen G, Chen Y, Zhang C. In-plane crashworthiness of bio-inspired hierarchical honeycombs. Compos Struct 2018;192:516–27.